

**Emergence of Robust High-Temperature Superconductivity in
 Li_3IrH_9 at Moderate Pressures**

Wendi Zhao¹, Shumin Guo¹, Tiancheng Mg¹, Zhengtao Liu¹, Chengda Li¹, Defang
Duan^{1*}, and Tian Cui^{1,2*}

¹State Key Laboratory of Superhard Materials, College of Physics, Jilin University,
Changchun 130012, China

²Institute of High Pressure Physics, School of Physical Science and Technology,
Ningbo University, Ningbo 315211, China

*Corresponding authors. duandf@jlu.edu.cn, cuitian@nbu.edu.cn

ABSTRACT

The discovery of near-room temperature superconductivity in compressed hydrides has sparked intensive efforts to find superconducting hydrides that are stable at low pressure or even ambient pressure. Herein, we present the ternary hydride Li_3IrH_9 as an exceptional candidate, which exhibits thermodynamic stability above 100 GPa and dynamic stability down to 8 GPa, exhibiting a superconducting transition temperature (T_c) of up to 113 K. In this structure, the broadening and overlapping between the electronic bands of the Ir-H antibonding states and the neighboring H ions result in the intrinsic metallicity of the hydrogen sublattice and drive the emergence of hydrogen-dominated significant electronic states at the Fermi level. Within this specific mechanism, the softened optical modes generated by hydrogen atoms encapsulated in the center of the Li octahedron play a critical role in strengthening electron-phonon coupling, an effect that remains robust even under high-pressures. Through high-throughput computational screening, we further identified a new family of superconductors derived from this prototype, including Li_3RhH_9 ($T_c = 124$ K at 20 GPa) and Li_3CoH_9 ($T_c = 80$ K at 10 GPa). This work provides original theoretical insights to accelerate the discovery of emerging hydride superconductor families that exhibit robust high-temperature superconductivity under moderate-pressures, along with promising potential for practical implementation.

Introduction

In recent years, compressed hydrides have emerged as a promising class of materials exhibiting high-temperature superconductivity, with some systems even demonstrating potential for room-temperature superconductivity, thereby attracting significant scientific attention. The remarkable superconducting properties of these materials originate from the chemical pre-compression effect induced by non-hydrogen elements, which enables hydrides to achieve superconducting states at pressures substantially lower than those required for solid molecular hydrogen[1,2]. Both theoretical and experimental studies have demonstrated that numerous binary hydrides, including prominent systems like H_3S [3-5], LaH_{10} [6-11], YH_6 [12,13], can achieve superconducting critical temperatures (T_c) beyond 200 K under high-pressure. Furthermore, theoretical predictions suggest that certain ternary clathrate hydrides, including $\text{Li}_2\text{MgH}_{16}$ [14], $\text{Li}_2\text{NaH}_{16}$, $\text{Li}_2\text{NaH}_{17}$ [15], $\text{LaSc}_2\text{H}_{24}$ [16], may exhibit superconducting transition temperatures surpassing room temperature. However, it is crucial to note that these remarkable superconducting properties are typically stabilized at extreme pressures above 150 GPa. This presents a significant challenge for practical applications, driving current research efforts to focus on the exploration of superconducting hydrides that can maintain their exceptional properties under moderate or even ambient pressure [17].

Notably, the modulation of H-H bonding motifs plays a crucial role in reducing the stable pressure of superconducting hydrides, which is dependent on the design of novel hydrogen motifs. For example, ternary clathrate hydrides (e.g., YCaH_{12} [18], YLuH_{12} [19] etc.) obtained through the substitution of typical binary structures still exhibit high stable pressures, often comparable to their binary parent structures. This phenomenon is primarily due to the lack of fundamental alterations in the H-H bonding characteristics. In contrast, LaBeH_8 , featuring a fluorite-type structure derived from the clathrate hydride LaH_{10} , demonstrates stability below megabar pressure, with an experimentally measured T_c of 110 K at 80 GPa [20,21]. Unlike the pure hydrogen cage lattice in LaH_{10} , the Be-H alloy lattice pre-compressed by La element can be sustained at significantly lower pressure. Additionally, LaBH_8 (154 K at 50 GPa),

BaSiH₈ (71 K at 3 GPa) and SrSiH₈ (126 K at 27 GPa) exhibit dynamic stability at moderate pressures[22-24]. Moreover, KB₂H₈ is predicted to host T_c up to 146 K at mild pressure of 12 GPa[25]. This compound can also be obtained by elemental substitution doping with LaH₁₀, resulting in BH₄ tetrahedral molecules embedded in the fcc potassium lattice. Similarly, RbB₂H₈ (101 K at 15 GPa)[26], MgC₂H₈ (55 K at 40 GPa)[27] and AlN₂H₈ (118 K at 40 GPa)[28], with analogous structures, are predicted to exhibit excellent superconductivity under moderate pressure.

Recently, advanced computational techniques, including machine-learning and high-throughput screening, have significantly accelerated the exploration of superconducting hydrides. Many predicted hydrides exhibit exceptional superconductivity at ambient pressure, such as Li₂CuH₆[29], Mg₂PtH₆[29], Mg₂IrH₆[29,30], with T_c exceeding the boiling point of liquid nitrogen. Although these hydrides possess relatively lower hydrogen content compared to metal superhydrides, they still demonstrate hydrogen-dominated superconducting behavior. For example, in Mg₂IrH₆, a hydrogen-dominated van Hove singularity emerges at the Fermi level, leading a strong electron-phonon coupling and a predicted maximum T_c of 160 K[29,30]. However, it is important to note that these hydrides are thermodynamically metastable, implying that their actual synthesis conditions may require high pressures. Determining the thermodynamic stability of such materials necessitates large-scale structural predictions to construct accurate thermodynamic phase diagrams—a critical step often overlooked high-throughput calculations.

Inspired by the excellent superconductivity of Mg₂IrH₆[30], we performed a large-scale structural prediction of the ternary Li-Ir-H system. This investigation led to the discovery of an unprecedented ternary hydride, Li₃IrH₉, which is thermodynamically stable above 100 GPa, and dynamically stable down to 8 GPa with T_c up to 113 K. The superior superconductivity of Li₃IrH₉ arises from its unique bonding characteristics. Specifically, the broadening and eventual overlapping of the H^{1a} atom (encapsulated within the Li octahedron) with the Ir-H antibonding electron band led to the metallization of the hydrogen sublattice, resulting in a hydrogen-dominated electron density of states at the Fermi level. Concurrently, the phonon modes of H^{1a} atoms

dominate the electron-phonon coupling and retain substantial contributions under reduced pressure, owing to the softening of these phonon modes. The predicted Li_3IrH_9 offers an unprecedented hydride structural prototype exhibiting robust high-temperature superconductivity, particularly given that many isotopic compounds have demonstrated excellent superconductivity at moderate pressures.

Results

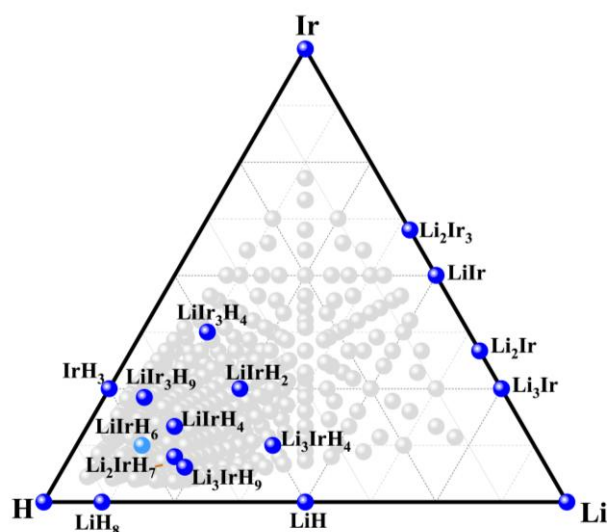


Figure 1 Ternary phase diagram of the Li-Ir-H system at 100 GPa. Green dots denote thermodynamically stable phases. Light green dots and gray dots represent metastable phases and structures far from convex hull, respectively.

We performed large-scale random structure prediction for the Li-Ir-H system at 50 GPa and 100 GPa using the AIRSS code [31,32], generating over 30,000 candidate structures. To construct the ternary phase diagram for assessing thermodynamic stability, we reproduced previously reported stable binary hydrides [33,34] and elemental solids[35-37] at the relevant pressures and discovered three novel stable alloys in the Li-Ir system: Li_3Ir , Li_2Ir , and Li_2Ir_3 . Figure 1 shows the ternary phase diagram of the Li-Ir-H system at 100 GPa, revealing seven thermodynamically stable phases: $Pm-3m$ LiIr_3H_4 , $P-62m$ LiIr_3H_9 , $P4/mmm$ LiIrH_2 , $C2/c$ LiIrH_4 , $I4/mmm$ Li_3IrH_4 , $I41/amd$ Li_2IrH_7 , $Pm-3m$ Li_3IrH_9 . We further assessed their dynamic stability threshold pressure and corresponding T_c values. Notably, the $Pm-3m$ Li_3IrH_9 maintain dynamic

stability down to 8 GPa, with a T_c of 113 K, significantly exceeding the boiling point of liquid nitrogen. With the increase of pressure, Li_3IrH_9 gradually approaches the convex hull, remaining within 51 meV of the convex hull above 50 GPa and achieving thermodynamic stability at pressures exceeding 100 GPa (see Figure S2). Importantly, Li_3IrH_9 exhibits significant energetic advantages across multiple synthesis pathways, indicating its high potential for successful synthesis (see Table S1). Metal alloys are extensively employed as precursors for synthesizing hydride superconductors under high-pressures. We propose the synthesis of Li_3IrH_9 through a precursor system consisting of Li_3Ir alloy and H_2 , with the calculated formation enthalpy being highly favorable at -0.486 eV/atom under 100 GPa. Remarkably, Li_3IrH_9 maintains a high T_c of 115 K even at 100 GPa. These results demonstrate its strong potential for high-pressure synthesis and its ability to retain high-temperature superconductivity at lower pressures due to exceptional dynamic stability.

Moreover, in the Li-Ir-H system, the dynamic stability threshold pressure of the other thermodynamically stable phases is about 50 GPa, however, their maximum T_c values are below 30 K. Among the metastable structures, $Fm-3m$ LiIrH_6 lies only 10 meV above the convex hull at 100 GPa and achieves high T_c of 134 K at 50 GPa. Given our objective of identifying high- T_c hydrides at moderate pressures, we will focus on investigating the superconductivity of Li_3IrH_9 and its potential isotypic compounds to elucidate the structure-property relationships in this class of hydrides.

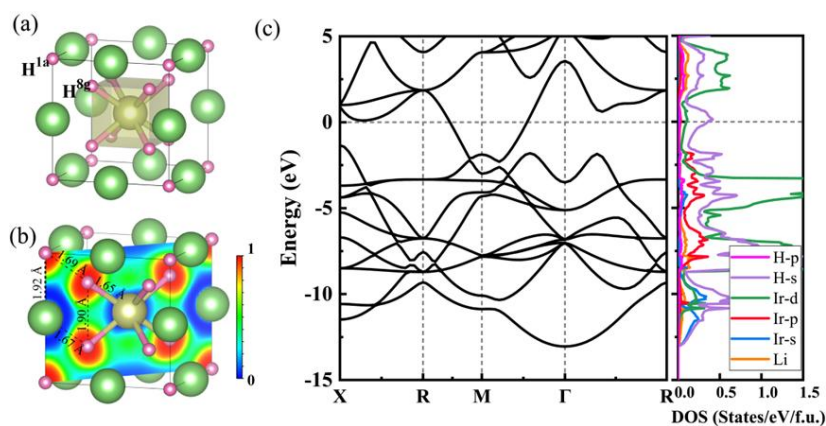


Figure 2 (a) Crystal structure, (b) electron localization function, (c) electronic band structure and density of states of $Pm-3m$ Li_3IrH_9 at 50 GPa.

The crystal structure of $Pm-3m$ Li_3IrH_9 is illustrated in Figure 2. In this structure, Li and Ir atoms occupy the 3d and 1b Wyckoff positions, respectively. The H atom (labeled H^{1a}), located at the 1a Wyckoff position, is encapsulated at the center of the Li octahedron, which can be viewed as a fragment of the $Fm-3m$ LiH lattice. Meanwhile, other H atoms (labeled H^{8g}) occupying the 8g Wyckoff positions form IrH_8 cubic unit around each Ir atom. At 50 GPa, the nearest-neighbor Li-H and Ir-H distances are 1.67 Å and 1.65 Å, respectively. The nearest-neighbor H-H distance is 1.69 Å, significantly longer than the bond length of the H_2 molecule (~ 0.74 Å) and even exceeding the typical H-H distances observed in clathrate hydride superconductors (1.1-1.3 Å)[38]. Metal atoms exhibit low electronegativity, with alkali metals serving as excellent electron donors. Bader charge analysis reveals that each Li and Ir atom donates electrons 0.83 |e| and 0.24 |e| to H atoms, respectively. The H^{1a} atom, being closer to more Li atoms, acquires 0.46 |e| per atom, which is higher than the 0.29 |e| obtained by each H^{8g} atom. Consequently, Li_3IrH_9 is expected to exhibit the bonding characteristics of ionic compounds, as further evidenced by the calculated electron localization function (Figure 1b). The notably low ELF values between Li and H atoms confirm the ionic nature of Li-H bonding. In contrast, the weak electron localization between Ir and H atoms suggests a mixed ionic-covalent bonding character. Interestingly, weak electron localization persists even between H atoms despite their large separation. The ELF value at the midpoint between the nearest H^{1a} and H^{8g} atoms is approximately 0.37, indicating weak covalent interaction and confirming the intrinsic metallicity of the hydrogen sublattice. This behavior mimics the electronic behavior of atomic metallic hydrogen, thereby facilitating phonon-mediated superconductivity—a feature distinct from purely ionic solids. For example, $Fm-3m$ LiH, a typical ionic solid, does not have any electron localization between H ions (see Figure S3). The electronic states derived from these isolated H-ions occupy the crystal orbitals below the Fermi level, accompanied by a wide band gap. Notably, metallization of LiH requires extremely high pressure, exceeding 300 GPa[39].

Figure 2c presents the electronic band structure and density of states (DOS) of

Li_3IrH_9 at 50 GPa. The localized DOS peak corresponding to Ir-d orbitals lies well below the Fermi energy, while hydrogen-derived states dominate the Fermi-level region, exhibiting a pronounced Van Hove singularity. Notably, the contributions of H atoms occupying different Wyckoff positions to the DOS near the Fermi level are significantly distinct. Each H^{1a} atom exhibits higher DOS contributions at the Fermi level compared to H^{8g} , with a distinct DOS peak adjacent to the Fermi level (see Figure S6). In contrast, the primary DOS peaks of H^{8g} atoms are localized between -10 eV and -5 eV, which is attributed to the strong hybridization between the Ir-d and H-s states in this region. This can be revealed more rigorously by atomic orbital symmetry analysis, that is, H^{8g} exhibits greater orbital symmetry matching with Ir atoms compared to H^{1a} , implying strong coupling (see Table S3). Additionally, the calculated crystal orbital Hamilton population (COHP) reveals that the Ir-H bond exhibits antibonding features near the Fermi level, with these diffuse antibonding orbitals extending along the Ir-H bond direction toward the H^{1a} site (see Figure S7) [40,41]. The metallization of hydrogen sublattices is primarily driven by the broadening and overlapping between the electronic bands of H^{1a} ions and Ir- H^{8g} antibonding states. Furthermore, the crystal orbitals occupying deeper energy levels are predominantly localized within the IrH_8 units, displaying significant bonding characteristics that further substantiate the covalent nature of Ir- H^{8g} interactions.

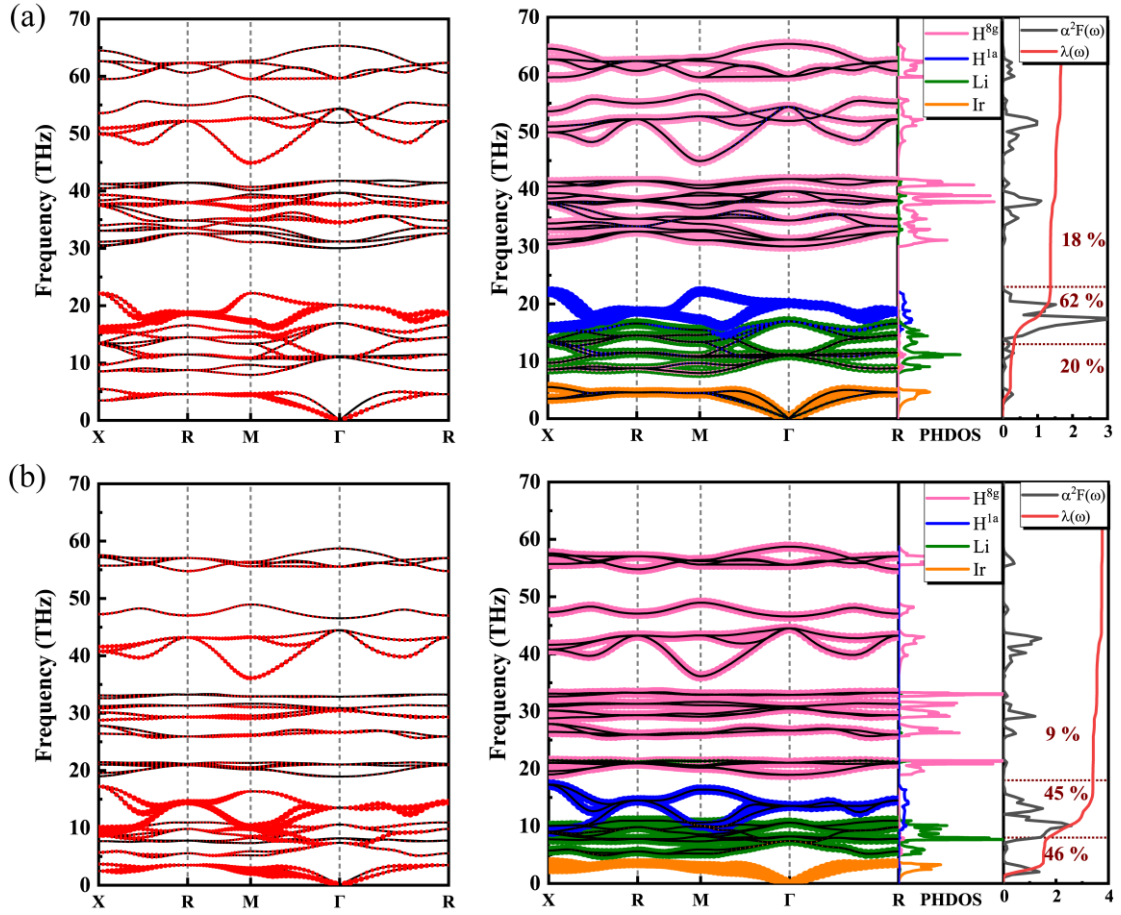


Figure 3 Phonon dispersion curves, projected phonon density of states (PHDOS), and Eliashberg spectral function $\alpha^2F(\omega)$ along with the electron-phonon integral $\lambda(\omega)$ for Li_3IrH_9 at (a) 50 GPa and (b) 8 GPa. The size of the red dots on the phonon dispersion curves represents the contribution of different phonon modes to the EPC, while the atomic-resolved phonon modes are also illustrated.

Figure 3 illustrates the phonon dispersion, projected phonon density of states (PHDOS), and Eliashberg spectral functions together with the electron-phonon integral $\lambda(\omega)$ of Li_3IrH_9 at 50 GPa and 8 GPa, providing insights into the origin of its high-temperature superconductivity. In the phonon spectrum, the acoustic modes and low-frequency optical modes are primarily dominated by Ir and Li atoms, respectively, while the intermediate and high-frequency optical phonon modes arise mainly from the vibrations of the lighter hydrogen atoms. The size of the red dots decorating the specific phonon modes represent their contribution to the EPC, with the largest contributions concentrated in the optical branches within the frequency range of 13–23 THz, accounting for about 62 % of the total EPC. This is further evidenced by the sharp peaks

in the Eliashberg spectral function within this range. Atom-resolved phonon dispersion curves reveal that these modes are predominantly associated the vibrations of the H^{1a} atom. For comparison, we also calculated the phonon dispersion of *Fm-3m* LiH at the same pressure, finding that the phonon frequency of H atom is higher (~ 40 THz), although it is also encapsulated in the center of Li octahedron (see Figure S8). This difference arises because the H^{1a} atom in Li₃IrH₉ acquires fewer electrons than the H atom in LiH and the Li-H^{1a} distance is longer, resulting in a weaker Li-H^{1a} ionic bond and consequently lower the phonon frequency. More importantly, the weak H-H interaction in Li₃IrH₉ influence the vibrational behavior of the hydrogen sublattice, which is significantly different from the high-frequency vibration of isolated H ions in LiH.

We further investigated the pressure dependence of phonon vibration frequency. As pressure decreases, the phonon vibration frequency decreases, especially at 8 GPa, where significant softening of optical branches and even acoustic branches enhances electron-phonon coupling. At this pressure, the phonon modes of the H^{1a} atoms and the Ir-dominated acoustic branch contribute almost equally to the total EPC (Figure 3b). Interestingly, the T_c of Li₃IrH₉ exhibits minimal pressure dependence, with values range from 104 K to 122 K over the pressure range of 8-150 GPa (Figure 4). This robust superconductivity contrasts with the general trend in hydride superconductors, where the T_c value decreases significantly with the increasing pressure. This is primarily attributed to the fact that the phonon modes of the H^{1a} atom consistently maintain a dominant contribution to electron-phonon coupling under varying pressure conditions. At the same time, we examined the pressure dependence of key superconducting parameters, including λ , ω_{log} , and N_{E_f} , which are generally positively correlated with T_c . Although increasing pressure leads to a reduction in both λ and N_{E_f} , the rise in ω_{log} is more pronounced. Moreover, the almost constant high ratio of PDOS_H at the Fermi level at different pressures suggests that the hydrogen vibrational modes remain the dominant factor governing superconductivity.

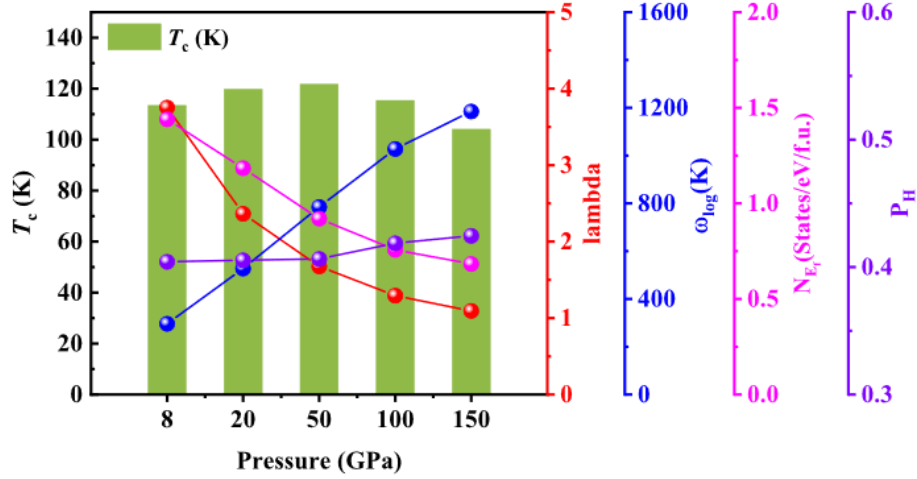


Figure 4 Calculated superconducting parameters of Li₃IrH₉ at different pressures. The obtained T_c using Eliashberg equation with $\mu^* = 0.1$ [42], the EPC parameter (λ), logarithmic average phonon frequency ω_{log} , the electronic density of states at the Fermi level $N(\epsilon_F)$, the contribution of H atoms DOS to the total DOS at the Fermi energy (P_H).

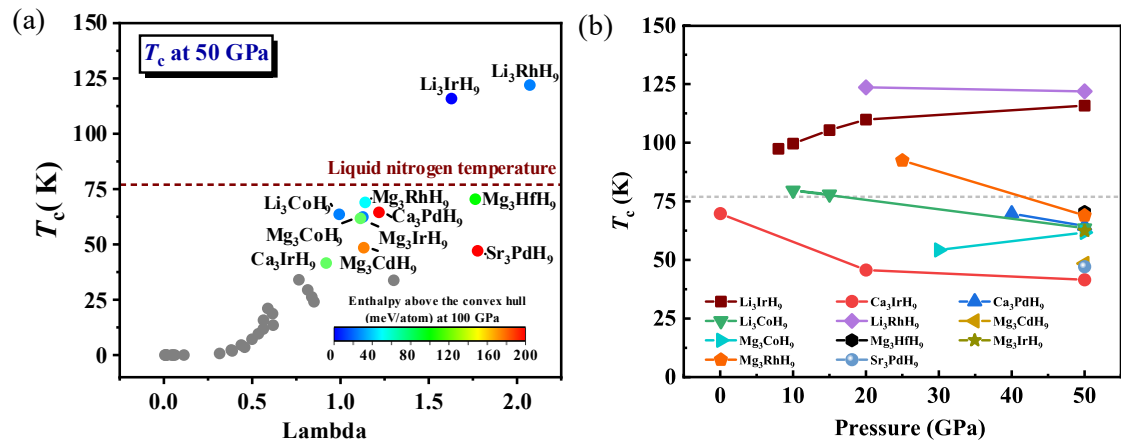


Figure 5 (a) High-throughput computational screening of A₃MH₉ (A = alkali/alkaline earth metal, M = transition metal) compounds at 50 GPa. Hydrides T_c higher than 40 K are labeled, with the color scale representing their thermodynamic stability (distance to the convex hull) at 100 GPa. The hydrides with T_c lower than 40 K are indicated by gray points by grey points. (b) Pressure-dependent T_c of A₃MH₉ hydrides, calculated using Allen-Dynes (AD) equation[43] with $\mu^* = 0.1$.

The remarkable stability and superior superconductivity of Li_3IrH_9 have inspired our comprehensive exploration of isostructural compounds within the A_3MH_9 family (A = alkali/alkaline earth metals; M = transition metals). We performed high-throughput calculations on 291 systems using our independently developed software package[44], identifying 36 dynamically stable structures at 50 GPa. Among these, 11 hydrides with T_c exceeding 40 K were selected for further investigation (Figure 5). We systematically evaluated the dynamic stability threshold pressure and thermodynamic stability of these 11 hydrides. While Li_3IrH_9 stands out as thermodynamically stable, the other isotopic compounds are thermodynamically metastable. Specifically, Li_3RhH_9 , Li_3CoH_9 , Mg_2IrH_6 and Mg_3RhH_9 are less than 70 meV/atom away from the convex hull at 100 GPa. Notably, Li_3RhH_9 , Li_3CoH_9 and Mg_3RhH_9 remain dynamically stable at pressures of 20, 10 and 25 GPa, respectively, with high T_c values of 124 K, 80 K and 92 K. Additionally, Ca_3IrH_9 is dynamically stable under ambient pressure and achieves a high T_c of 70 K. The variations in superconductivity among these hydrides can be attributed to the influence of A and M elements, whose differing electronegativities and atomic radii modulate the electronic structure near the Fermi level. Alkali and alkaline earth metals such as Li and Mg are preferred for the A site, while transition metals close to Ir in the periodic table are favored for the M site. For instance, Li_3RhH_9 exhibits an electronic structure similar to Li_3IrH_9 , with hydrogen dominating the electronic DOS at the Fermi level. In contrast, the DOS at the Fermi level in Li_3CoH_9 mainly comes from the Co- d states, which relatively suppresses the superconductivity (Figure S11). In fact, for A_3MH_9 systems with low T_c , the d states of transition metals often contribute significantly to the electron density of states at the Fermi level, highlighting the critical role of electronic structure in determining superconducting behavior.

Conclusion

In summary, our theoretical investigation has identified a series of thermodynamically stable hydrides in the Li-Ir-H system, with Li_3IrH_9 emerging as an excellent superconducting material under moderate pressure. This compound achieves a high T_c of 113 K under dynamically stable pressure at 8 GPa, maintaining a

consistently high T_c of 115 K even under thermodynamically stable pressure at 100 GPa. The robust superconductivity of Li_3IrH_9 can be attributed to its unique bonding characteristics, where the Ir-H bond exhibits a distinctive ion-covalent hybrid interaction. This interaction, particularly through the broadening and overlapping of the Ir-H antibonding electron band with adjacent H atoms, leads to the metallization of the hydrogen sublattice. This structural feature not only generates hydrogen-dominated electron density of states at the Fermi level but also significantly enhances electron-phonon coupling through the softening of hydrogen phonon modes. Strikingly, Li_3IrH_9 represents the prototype of an unprecedented hydride superconductor family with the general formula A_3MH_9 (A=alkali/alkaline earth metal, M=transition metal). Isostructural compounds, such as Li_3RhH_9 , Li_3CoH_9 , and Mg_3RhH_9 , also exhibit superior superconductivity, with maximum T_c values exceeding liquid nitrogen temperature below 50 GPa. These findings provide valuable insights into the development of superconducting hydrides with practical applications and open new avenues for obtaining high-temperature superconductivity in hydrides at moderate or even ambient pressures.

Acknowledgements

This work was supported by the National Key Research and Development Program of China (No. 2023YFA1406200 and No. 2022YFA1402304), the National Natural Science Foundation of China (Grants No. 12274169, No. 12122405, and No. 52072188), the Program for Science and Technology Innovation Team in Zhejiang (No. 2021R01004), and the Fundamental Research Funds for the Central Universities. Some of the calculations were performed at the High-Performance Computing Center of Jilin University and using TianHe-1(A) at the National Supercomputer Center in Tianjin.

- [1] M. I. Eremets, A. P. Drozdov, P. P. Kong, and H. Wang, *Nat Phys* **15**, 1246 (2019).
- [2] N. W. Ashcroft, *Phys. Rev. Lett.* **92**, 187002 (2004).
- [3] D. F. Duan *et al.*, *Sci. Rep.* **4**, 6968, 6968 (2014).
- [4] A. P. Drozdov, M. I. Eremets, I. A. Troyan, V. Ksenofontov, and S. I. Shylin, *Nature* **525**, 73 (2015).
- [5] D. F. Duan, X. L. Huang, F. B. Tian, D. Li, H. Y. Yu, Y. X. Liu, Y. B. Ma, B. B. Liu, and T. Cui, *Phys. Rev. B* **91**, 180502, 180502 (2015).
- [6] H. Y. Liu, Naumov, II, R. Hoffmann, N. W. Ashcroft, and R. J. Hemley, *Proc. Natl. Acad. Sci. U. S. A.* **114**, 6990 (2017).
- [7] F. Peng, Y. Sun, C. J. Pickard, R. J. Needs, Q. Wu, and Y. M. Ma, *Phys. Rev. Lett.* **119**, 107001, 107001 (2017).
- [8] A. P. Drozdov *et al.*, *Nature* **569**, 528 (2019).
- [9] Z. M. Geball, H. Liu, A. K. Mishra, and M. Ahart, *Angew. Chem. Int. Ed.* **57**, 688 (2018).
- [10] M. Somayazulu, M. Ahart, A. K. Mishra, Z. M. Geballe, M. Baldini, Y. Meng, V. V. Struzhkin, and R. J. Hemley, *Phys. Rev. Lett.* **122**, 027001, 027001 (2019).
- [11] F. Hong *et al.*, *Chin. Phys. Lett.* **37**, 107401 (2020).
- [12] I. A. Troyan *et al.*, *Adv. Mater.* **33**, 2006832 (2021).
- [13] P. Kong *et al.*, *Nat. Commun.* **12**, 5075 (2021).
- [14] Y. Sun, J. Lv, Y. Xie, H. Liu, and Y. Ma, *Phys. Rev. Lett.* **123**, 097001 (2019).
- [15] D. An, D. Duan, Z. Zhang, Q. Jiang, H. Song, and T. Cui, *arXiv:2303.09805* (2023).
- [16] X.-L. He, W. Zhao, Y. Xie, A. Hermann, R. J. Hemley, H. Liu, and Y. Ma, *Proc. Natl. Acad. Sci. U. S. A.* **121**, e2401840121 (2024).
- [17] W. Zhao, X. Huang, Z. Zhang, S. Chen, M. Du, D. Duan, and T. Cui, *Natl. Sci. Rev* **11**, nwad307 (2024).
- [18] W. Zhao, D. Duan, M. Du, X. Yao, Z. Huo, Q. Jiang, and T. Cui, *Phys. Rev. B* **106**, 014521 (2022).
- [19] M. Du, H. Song, Z. Zhang, D. Duan, and T. Cui, *Research* **2022**, 9784309 (2022).
- [20] Z. Zhang *et al.*, *Phys. Rev. Lett.* **128**, 047001 (2022).
- [21] Y. Song, J. Bi, Y. Nakamoto, K. Shimizu, H. Liu, B. Zou, G. Liu, H. Wang, and Y. Ma, *Phys. Rev. Lett.* **130**, 266001 (2023).

- [22] X. Liang *et al.*, Phys. Rev. B **104**, 134501 (2021).
- [23] S. Di Cataldo, C. Heil, W. von der Linden, and L. Boeri, Phys. Rev. B **104**, L020511 (2021).
- [24] R. Lucrezi, S. Di Cataldo, W. von der Linden, L. Boeri, and C. Heil, npj Comput. Mater. **8**, 119 (2022).
- [25] M. Gao, X.-W. Yan, Z.-Y. Lu, and T. Xiang, Phys. Rev. B **104**, L100504 (2021).
- [26] S. Li, H. Wang, W. Sun, C. Lu, and F. Peng, Phys. Rev. B **105**, 224107 (2022).
- [27] M. Jiang, Y. Hai, H. Tian, H. Ding, Y. Feng, C. Yang, X. Chen, and G. Zhong, Phys. Rev. B **105**, 104511 (2022).
- [28] Z. Wan and R. Zhang, Appl. Phys. Lett. **121**, 192601 (2022).
- [29] T. F. T. Cerqueira, Y.-W. Fang, I. Errea, A. Sanna, and M. A. L. Marques, Adv. Funct. Mater. **34**, 2404043 (2024).
- [30] K. Dolui, L. J. Conway, C. Heil, T. A. Strobel, R. P. Prasankumar, and C. J. Pickard, Phys. Rev. Lett. **132**, 166001 (2024).
- [31] C. J. Pickard and R. J. Needs, Phys. Rev. Lett. **97**, 045504 (2006).
- [32] C. J. Pickard and R. J. Needs, J. Phys. Condes. Matter **23**, 053201, 053201 (2011).
- [33] Y. Xie, Q. Li, A. R. Oganov, and H. Wang, Acta Crystallogr C **70**, 104 (2014).
- [34] T. Scheler, M. Marqués, Z. Konôpková, C. L. Guillaume, R. T. Howie, and E. Gregoryanz, Physical Review Letters **111**, 215503 (2013).
- [35] C. J. Pickard and R. J. Needs, Nature Physics **3**, 473 (2007).
- [36] N. A. Smirnov, Journal of Applied Physics **134**, 025901 (2023).
- [37] J. Lv, Y. Wang, L. Zhu, and Y. Ma, Physical Review Letters **106**, 015503 (2011).
- [38] Y. Sun, X. Zhong, H. Liu, and Y. Ma, Natl. Sci. Rev **11**, nwad270 (2024).
- [39] E. Zurek, R. Hoffmann, N. W. Ashcroft, A. R. Oganov, and A. O. Lyakhov, Proc. Natl. Acad. Sci. U. S. A. **106**, 17640 (2009).
- [40] S. Maintz, V. L. Deringer, A. L. Tchougréeff, and R. Dronskowski, J Comput Chem **37**, 1030 (2016).
- [41] V. L. Deringer, A. L. Tchougréeff, and R. Dronskowski, J. Phys. Chem. A **115**, 5461 (2011).
- [42] G. M. Eliashberg, Sov. Phys. JETP **11**, 696 (1960).
- [43] P. B. Allen and R. C. Dynes, Phys. Rev. B **12**, 905 (1975).
- [44] T. Ma, Z. Zhang, S. Wu, D. Duan, and T. Cui, arXiv preprint arXiv:2502.04984 (2025).